A Turbulent Wall-Pressure Fluctuation Model for Fluid-Structure Interaction

M. Zhang[*] and A. Frendi[*]
Corresponding author: frendik@uah.edu

*University of Alabama in Huntsville, USA

Abstract: Most fluid flows of practical applications are turbulent. In flows involving interactions with flexible structures, such as an aircraft skin, the knowledge of turbulent wall-pressure fluctuations is critical. Both measurements and direct numerical simulations of the wall-pressure fluctuations are difficult and costly. Therefore, the use of semi-empirical turbulent wall-pressure fluctuation models is wide spread. One of the most widely used models is that due to Corcos (1963). The biggest advantages of this model are; simplicity and ease of use. However, the model has several weaknesses as well and therefore many models have been proposed to address them. In this paper, we briefly review existing models and then propose a model that remedies their weaknesses. The proposed model keeps the simplicity of the Corcos model and it is given in both space-frequency and wavenumber-frequency spaces. The new model accurately captures the convective peak and shows better agreement with experimental data at lower wavenumbers.

Keywords: Turbulent Wall-Pressure Fluctuations, Wavenumber-Frequency, Space-Frequency, Fluid-Structure Interaction.

1   Introduction

For flows over flexible structures, the knowledge of the turbulent wall-pressure fluctuations is critical for accurate determination of structural vibration and the resulting acoustic radiation. For the aircraft industry, both interior and exterior noises are of great importance to future growth. Reduction of interior noise is important for passenger comfort, while reducing exterior noise will help alleviate the noise pollution in airport communities which have become very vocal of late. Since wall-pressure fluctuations are required to determine structural vibrations and hence interior noise, many researchers have attempted to either measure, model or compute them. Early measurements of turbulent wall pressure fluctuations were performed by Willmarth and Wooldridge (1962) who used the space-time correlations technique developed by Favre et al. (1957). Willmarth and Wooldridge (1963) extended the space-time correlation measurements of the wall pressure to that between wall pressure and two velocity components. Corcos (1963) proposed, after a detailed analysis of Willmarth and Wooldridge data, a semi-empirical model for the cross-spectral density function as a function of frequency and separation distances in the cross-flow and flow directions. This model has since become the most useful model for coupling the interaction between fluids and structures.

1

Ffowcs William (1982) and Dowling (1992) tried to extend Corcos' model to the low wavenumber region, however their efforts resulted in more complex models with unknown constants. Hwang and Geib (1984) proposed a simplified version to the Ffowcs Williams model, however Graham (1997) concluded after testing several models for acoustic radiation from vibrating plates that Hwang and Geib's model was not adequate. Efimtsov (1982) modified the Corcos model by taking into account the dependence of spatial correlation on boundary layer thickness and spatial separation. The model was designed for aircraft applications and has parameters that depend on Mach number. Similar to Corcos', the model's weakness is at low wavenumbers. Smol'yakov and Thachenko (1991) modified the Corcos model to make the coherence contours in the space-frequency space into elliptic curves and to improve Corcos' predictions at low wavenumbers. Chase (1987) improved on his own earlier model (1980) and that of Corcos when compared to experimental data, however the wavenumber white characteristic of experimental observations at low wavenumbers was not reproduced. More recently, Caiazzo et al. (2016) proposed a generalized Corcos-like model that allowed controlling the decay in the wavenumber domain below the convective peak while preserving its mathematical advantages.

The importance of wall pressure fluctuations to various engineering application has led a large number of research papers some of which have not been mentioned in this brief introduction. In order to keep up with the advancement of the field, several literature reviews have been published starting from Willmarth (1975) to Eckelmann (1988) then Bull (1996) and more recently Juve (2015). These reviews are critical in that they update the state of advancement in the field and set the stage for future research efforts.

2   Problem Statement

Estimating the statistical properties of the wall-pressure-fluctuations (WPF) in a turbulent boundary layer is of critical importance to many practical engineering applications. One such application is flow induced vibration and noise radiation both interior and exterior to a given vehicle. It is well-known that the necessary and sufficient information for the WPF is given by the space-time covariance function defined as

$$R_{pp}(\zeta, \eta, \tau) = <p(x_1, x_2, t)p(x_1 + \zeta, x_2 + \eta, t + \tau)>. \qquad (1)$$

with (ζ, η) being the separation distances in the (x_1, x_2) directions and τ being the separation in time. In most applications, it is the Fourier transform of Equation (1) that is desired, i.e. the wavenumber-frequency spectrum, $\hat{R}_{pp}(k_1, k_2, \omega)$, or the cross spectrum, i.e. the space-frequency spectrum, $R_{pp}^*(\zeta, \eta, \omega)$. The coordinate system used in this paper is shown on Figure 1 with $\vec{e}_1$ being the streamwise, $\vec{e}_2$ the cross-flow and $\vec{e}_3$ the wall normal directions, respectively. The arrow on the left side of the figure shows the flow direction.
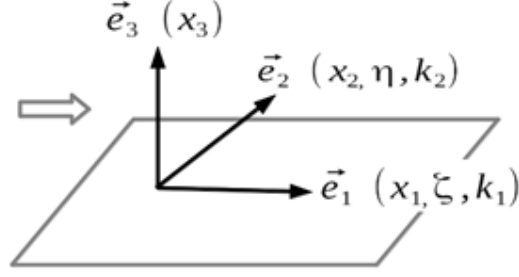
Figure 1: Coordinate system used.

One of the earliest and most widely used models was due to Corcos (1963), who proposed a cross-spectral density of the form

$$R^*_{pp}(\zeta, \eta, \omega) = R^*_{pp}(\omega) A\left(\frac{\omega\zeta}{U_c}\right) B\left(\frac{\omega\eta}{U_c}\right) e^{j\omega\zeta/U_c} \tag{2}$$

Where $R^*_{pp}(\omega)$ is the auto-spectrum, U_c the convection velocity and A and B are functions of the similarity variables $\left(\frac{\omega\zeta}{U_c}\right)$ and $\left(\frac{\omega\eta}{U_c}\right)$ and are of the form

$$A\left(\frac{\omega\zeta}{U_c}\right) = e^{-\alpha\frac{\omega|\zeta|}{U_c}}, \qquad B\left(\frac{\omega\eta}{U_c}\right) = e^{-\beta\frac{\omega|\eta|}{U_c}} \quad \text{with } \alpha \sim 0.1 - 0.19 \text{ and } \beta \sim 0.7 - 1.2. \tag{3}$$

The coherence is given by

$$\frac{|R^*_{pp}(\zeta, \eta, \omega)|}{R^*_{pp}(\omega)} = A\left(\frac{\omega\zeta}{U_c}\right) B\left(\frac{\omega\eta}{U_c}\right). \tag{4}$$

In order to obtain the wavenumber-frequency spectrum, one needs to take the Fourier transform of Equation (2) to arrive at

$$\hat{R}_{pp}(k_1, k_2, \omega) = \frac{1}{\pi^2}\left(\frac{U_c}{\omega}\right)^2 R^*_{pp}(\omega) \frac{\alpha\beta}{[\alpha^2 + (\frac{k_1 U_c}{\omega} - 1)^2][\beta^2 + (\frac{k_2 U_c}{\omega})^2]}. \tag{5}$$

The simplicity and ease of use of the Corcos model led to its extensive use in many engineering applications involving structural vibrations. However, the Corcos model has many shortcomings such as the overestimate of the spectrum level at low wavenumbers and the innacurate shape of the coherence contours predicted by the model.

2.1 Wall Pressure Fluctuation Model

In this paper, a new model for the wall pressure fluctuations is proposed that keeps the simplicity of the Corcos model but corrects some of its shortcomings. The proposed model uses prior research results of Singer (1996b) who showed that the coherence contours obtained from Large Eddy Simulation computations were ellipses while those given by the Corcos models were straight lines (see proof in Appendix A). The new model uses experimental results to anchor the low wavenumber spectral level predicted
.

We start by writing the generalized wavenumber vector as

$$\vec{k} = k_1\vec{e}_1 + k_2\vec{e}_2 + k_\omega\vec{e}_\omega \tag{6}$$

where $k_\omega\vec{e}_\omega$ represents the contribution from frequency in the direction of the convection velocity, U_c, which is $\vec{e}_1$. This leads to $k_\omega\vec{e}_\omega = -\frac{\omega}{U_c}\vec{e}_1$ and hence

$$\vec{k} = \left(k_1 - \frac{\omega}{U_c}\right)\vec{e}_1 + k_2\vec{e}_2. \tag{7}$$

Equation 7 shows that the wavenumber vector is centered on the convective ridge where most of the flow energy resides.

Based on direct numerical simulation results of Choi and Moin (1990) and large eddy simulation results of Singer (1996b) and Viazzo et al. (2001), we propose a wavenumber-frequency spectrum, $\hat{R}_{pp}(k_1, k_2, \omega)$, that satisfies the following conditions; (1) $\hat{R}_{pp}(k_1, 0, \omega)$ should match Efimtsov's prediction around the convective peak for all frequencies, (2) $\hat{R}_{pp}(k_1, 0, \omega)$ should agree with experimental data at low wavenumbers and (3) the coherence contours should be elliptic in shape. With those conditions, we propose a spectrum of the form

$$\hat{R}_{pp}(k_1, k_2, \omega) = C_1 R_{pp}^*(\omega)e^{-\tilde{\alpha}r_k} \tag{8}$$

with $\tilde{\alpha} = \alpha\delta$ where α is an empirical constant and δ the boundary layer thickness. In Equation (8), C_1 is a constant, $R_{pp}^*(\omega)$ is the auto-spectrum and r_k is such that

$$|r_k|^2 = \left[k_1 - \left(\frac{\omega}{U_c}\right)\right]^2 + (mk_2)^2 \qquad \text{with } m \text{ being the scaling factor obtained by}$$

minimizing the error given by

$$E(m, \omega) = \int_0^{k_{1cutoff}} \left[\hat{R}_{pp}(k_1, 0, \omega) - \hat{R}_{pp}(0, \frac{k_1}{m}, \omega)\right]^2 dk_1 \ . \tag{9}$$

A similar expression was used by Singer (1996b). The cross-spectrum can be obtained by taking the inverse Fourier transform of Equation (8)

$$R_{pp}^*(\zeta, \eta, \omega) = \iint \hat{R}_{pp}(k_1, k_2, \omega)e^{j(k_1\zeta + k_2\eta)}dk_1dk_2. \tag{10}$$

Integrating using complex variables results in (see Appendix B)

$$R_{pp}^*(\zeta, \eta, \omega) = 2\pi\frac{C_1}{m\delta^2}R_{pp}^*(\omega)e^{j\frac{\omega}{U_c}\zeta}\frac{\alpha}{\left[\alpha^2 + \left(\frac{\eta}{\delta m}\right)^2 + \left(\frac{\zeta}{\delta}\right)^2\right]^{3/2}} . \tag{11}$$

For $\zeta = \eta = 0$, one can get the auto-spectrum

$$R_{pp}^*(0, 0, \omega) = R_{pp}^*(\omega) = 2\pi\frac{C_1}{m\delta^2}R_{pp}^*(\omega)\frac{1}{\alpha^2} \tag{12}$$

leading to

$$C_1 = \alpha^2 m\delta^2\frac{1}{2\pi}. \tag{13}$$

The cross-spectrum is therefore given by

$$R_{pp}^*(\zeta, \eta, \omega) = R_{pp}^*(\omega)e^{j\frac{\omega}{U_c}\zeta} \frac{\alpha^3}{\left[\alpha^2 + \left(\frac{\eta}{\delta m}\right)^2 + \left(\frac{\zeta}{\delta}\right)^2\right]^{3/2}}. \tag{14}$$

With m obtained from

$$E(m, \omega) = \int_0^{\zeta_{cutoff}} \left[R_{pp}^*(\zeta, 0, \omega) - R_{pp}^*(0, m\zeta, \omega)\right]^2 d\zeta. \tag{15}$$

2.1.1   Empirical Constants

We first focus on the decay coefficient α. Using experimental results of Farabee and Casarella (1991), Abraham and Keith (1998), Leclercq and Bohineust (2002) and the direct numerical simulation results of Choi and Moin (1990) it can be shown that the auto-spectra for different freestream velocities collapse when nondimensionalized using a combination of inner and outer variables; τ_w, u_τ and δ; such that $\hat{R}_{pp}(\omega)u_\tau/\tau_w^2\delta$ for auto-spectra and $\omega\delta/u_\tau$ for frequency. The nondimensionalized auto-spectra exhibit a peak around $\frac{\omega\delta}{u_\tau} \sim 50$. In addition, using Efimtsov (1982) who modified the Corcos model to include the boundary layer thickness using flight data, we arrived at a decay coefficient of the form

$$\alpha = \frac{1}{\pi} \frac{a_1}{\sqrt{1.0 + a_2\left(\frac{\omega\delta}{u_\tau} - \frac{\omega_m\delta}{u_\tau}\right)^2}} \tag{16}$$

where $\frac{\omega_m\delta}{u_\tau} \sim 50$ and (a_1, a_2) are obtained for conditions (1), (2) and (3) given for Equation (8). In this paper, the following parameters are used; $a_1 = 4.7$ and $a_2 = 3.0e^{-5}$ and the scaling factor, m, for a zero-pressure gradient turbulent boundary layer flow is $m \sim \frac{1}{7.7}$ or $\frac{1}{7.8}$.

For the choice of the auto-spectra, Figure 2 shows that only the model proposed by Goody (2004), red-line, comes close to the experimentally obtained auto-spectrum of Farabee and Casarella (1991), black line with dots. The Chase (1987) model, green-dash, and the Smolyakov and Tkachenko (1991) model, blue-dot, are not as accurate. Therefore, in the current study we choose to use Farabee and Casarella (1991) auto-spectrum in our model and that of Corcos and Efimtsov. For the other models the built-in or model-specific auto-spectrum is used.
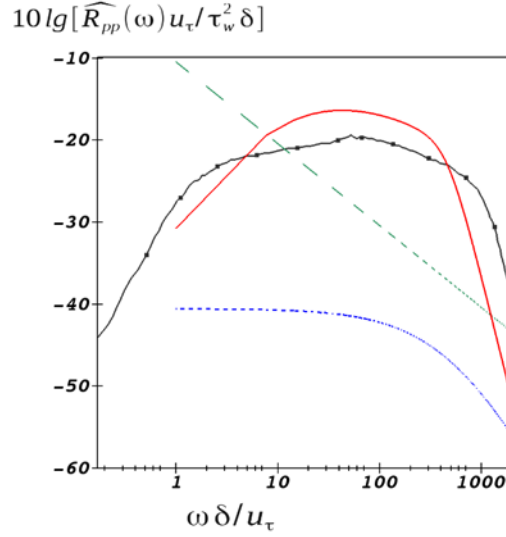
Figure 2: Comparison of normalized auto-spectra; Farabee and Casarella experiments (1991), black line with dots; Chase model (1991), green-dashes, Goody model (2004), red-line, Smol'yakov and Tkachenko model (1991), blue-dots.

3   Results and Discussion

3.1   Three Dimensional Wavenumber-Frequency Spectra

Figure 3 show a comparison of the proposed three dimensional wavenumber-frequency spectra, $\hat{R}_{pp}(k_1, 0, \omega)$, to that of Corcos (1963), Efimtsov (1982), Chase (1987), Smol'yakov and Tkachenko (1991) and Witting (1986). The experimental results of Martin and Leehey (1977) and Smol'yakov and Tkachenko (1991) are also included in the plot. The wavenumber-frequency spectra are normalized by $\tau_w^2 \delta^3/u_\tau$, the dimensionless frequency used is $\frac{\omega\delta}{u_\tau} = 509$ or $\frac{\omega\delta^*}{U_\infty} = 2.1$. The choice of flow quantities follow Smol'yakov and Tkachenko (1991); $\frac{\delta}{\delta^*} = 8, \frac{u_\tau}{U_\infty} = 0.033$ and $\frac{U_c}{U_\infty} = 0.8$; with (δ, δ^*) being the boundary layer and displacement thicknesses, respectively; and (U_∞, U_c, u_τ) being the freestream, convection and friction velocities, respectively. For Witting's model, it was assumed that $C = 10$, $\frac{\delta_{min}}{\delta^*} = 0.08, \frac{\delta_{max}}{\delta^*} = 0.6$ and $< p^2 >/\tau_w^2 = 8.0$. For the Corcos model, $\alpha = 0.11$ and $\beta = 0.77$. Figure 3(a) is obtained for a dimensionless frequency of $\frac{\omega\delta}{u_\tau} = 509$ ($\frac{\omega\delta^*}{U_\infty} = 2.1$), while Figure 3(b) is obtained for $\frac{\omega\delta}{u_\tau} = 727$ ($\frac{\omega\delta^*}{U_\infty} = 3.0$). In Figure 3b, the experimental results shown in the box originate from Martin and Leehey's (1977) and Martini et al. (1984).

Figure 3 show that our proposed model captures the convective peak accurately and is in agreement with all experimental data sets included on both plots. In the low wavenumber area, our model predicts 20-30 dB lower levels than those predicted by Corcos' and Efimtsov's. The Chase model is the only model that is not wavenumber white below the convection peak; instead it decreases rapidly to zero at low wavenumbers as reported by other investigators.
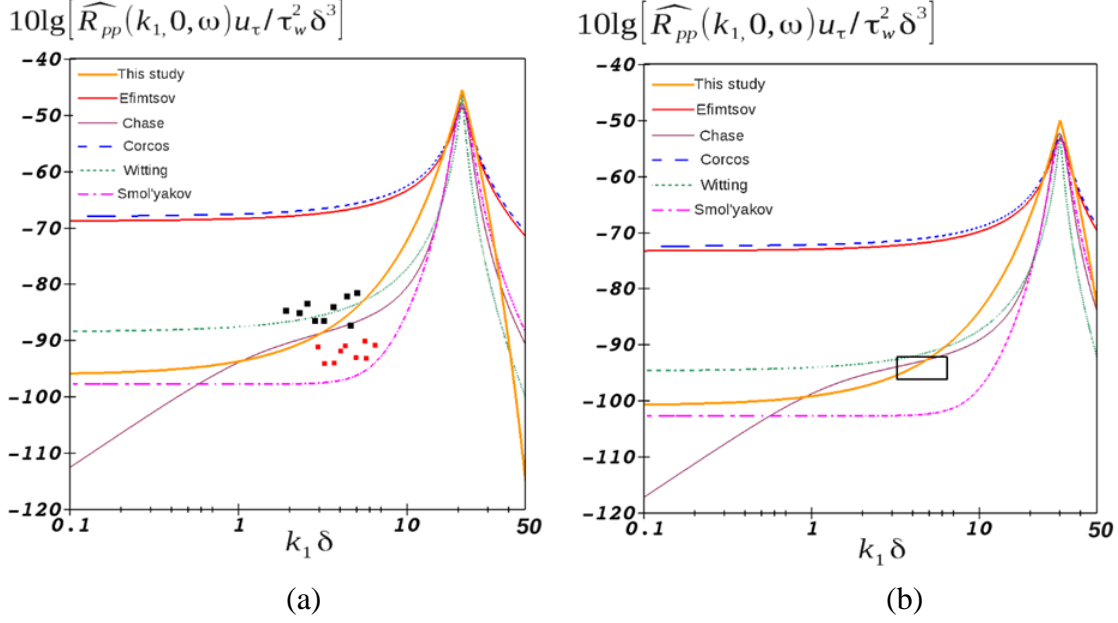
6

Figure 3: Comparison of normalized three dimensional wavenumber-frequency spectra obtained using our proposed model to other select models from the literature. (a), $\frac{\omega\delta}{u_\tau} = 509$ and the squares represent experimental data obtained for $\frac{\omega\delta}{u_\tau} = 436.36 \sim 557.58$ ($\frac{\omega\delta^*}{U_\infty} = 1.8 \sim 2.3$). Black square are data from Tkachenko et al. (2008) and red squares are from Smol'yakov and Tkachenko (1991). (b), $\frac{\omega\delta}{u_\tau} = 727$ and the black box represents the locus of the data from Martin and Leehey (1977) and Martini et al. (1984).

Figure 4(a)-(d) show comparisons of our proposed three dimensional wavenumber-frequency spectrum to those in the literature for $\frac{\omega\delta}{u_\tau} = 142.35$. The flow quantities used for Figure 4(a) are those from Viazzo et al. (2001); $\frac{u_\tau}{U_\infty} = 0.048$, $\frac{U_c}{U_\infty} = 0.65$.; and for Witting's model $C = 7$, $\frac{z_{min}}{\delta^*} = 0.65$ and $\frac{z_{max}}{\delta^*} = 0.65$. Most models are in agreement with the LES results of Viazzo et al. (2001) around the convective peak, however, disagreements show up on either side of the peak. On the low wavenumber side, our model and that of Smol'yakov and Tkachenko (1991) show a much better agreement with the LES results. Corcos' and Efimtsov models overestimate the spectrum level by as much as 30 dB. For Figure 4(b)-(d), the nondimensional frequency, $\omega\delta/u_\tau$, varies from 24.8 to 248 and the flow quantities used are those from Smol'yakov and Tkachenko (1991). At a low nondimensional frequency of 24.8, Figure 4(b), the influence of the boundary layer thickness becomes important. The shape of the Corcos model spectrum is unchanged as it is independent of the boundary layer thickness, while that of Efimtsov becomes broader with a lower level peak. Our model spectrum is in agreement with that of Efimtsov near and below the peak, as expected. The other spectra show a prominent convective peak similar to Corcos' with Witting spectrum having the highest level and sharpest peak. As the nondimensional frequency is increased to 85, Figure 4(c), a lower level convective peak is predicted by the Efimtsov model, while our model predicts a sharper higher level peak. All other models predict a prominent convective peak with a higher level. Note that the Efimtsov model spectrum is approaching that of Corcos away from the convective peak. Our model exhibits lower levels on both sides of the peak.

As the nondimensional frequency is increased to 248, Figure 4(d), the convective peak becomes prominent and both the Corcos and Efimtsov models predict nearly the same spectrum across all wavenumbers. Our model predicts the same convective peak with slightly higher level, however on the low wavenumber side of the peak, our model predicts levels that are much lower than that of Corcos' and Efimtsov's. The other models also show lower levels away from the peak. The Chase model predicts a rapid decrease in level at low wavenumbers.
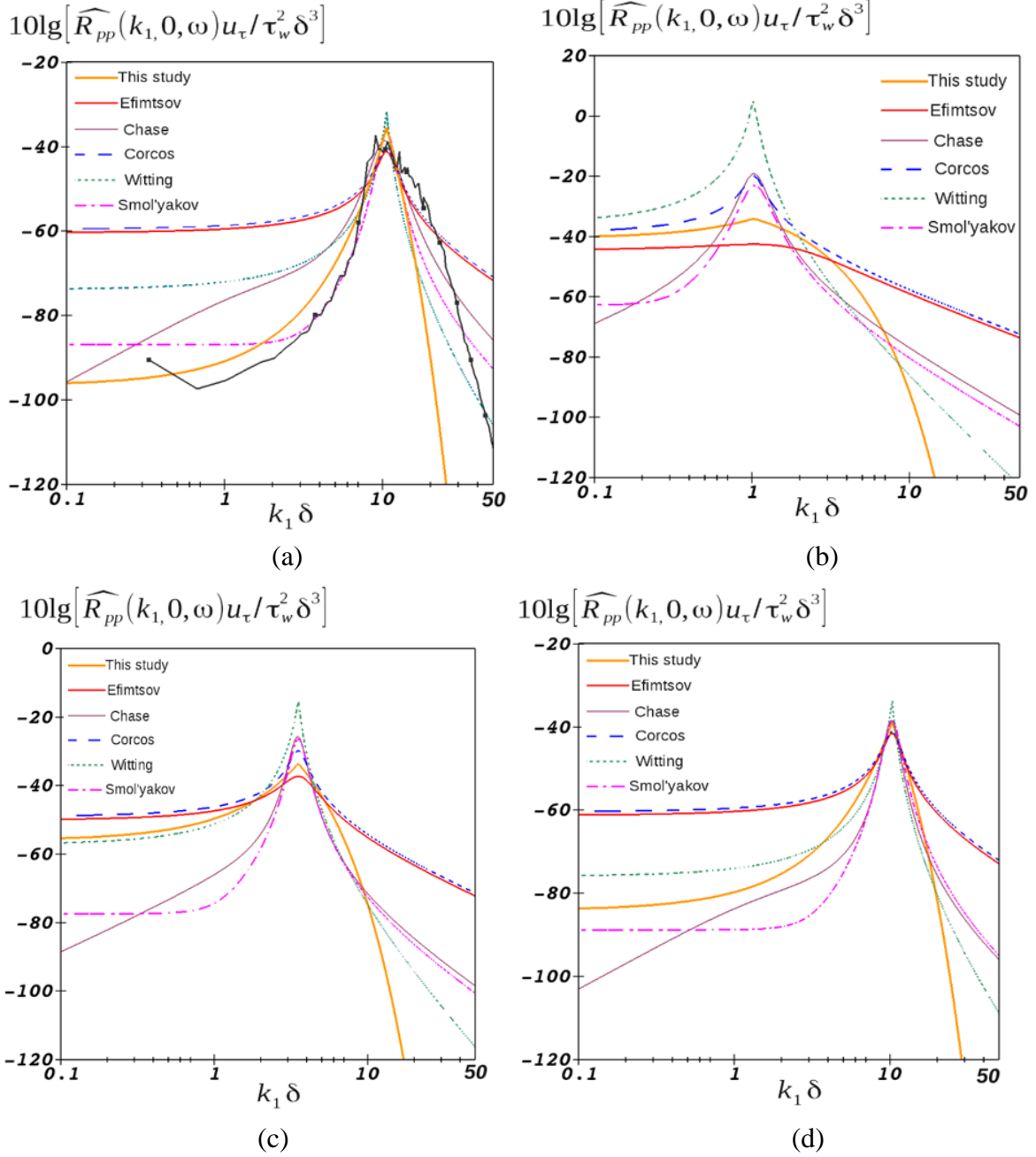

Figure 4: Comparison of three dimensional wavenumber-frequency spectra. (a) $\frac{\omega\delta}{u_\tau} = 142.35$, the black line with symbols represents LES results from Viazzo et al. (2001), (b) $\frac{\omega\delta}{u_\tau} = 24.8$, (c) $\frac{\omega\delta}{u_\tau} = 85$ and (d) $\frac{\omega\delta}{u_\tau} = 248$.

Figures 3 and 4 cover a nondimensional frequency range of $\frac{\omega \delta}{u_\tau} = 24.8$ to 727. For all the nondimensional frequencies, the Corcos model exhibits the same shape: a prominent convective peak with a higher level spectrum at low wavenumbers. Our model captures the convective peak accurately at all frequencies and predicts lower spectral levels at low wavenumbers. Our proposed spectrum shows a dependence on boundary layer thickness at low frequencies similar to Efimtsov's.

3.2 Low Wavenumber Spectral Level

For low speed and/or underwater applications, the low wavenumber range of the spectrum is very important. Therefore accurate prediction of the spectral level is critical in these applications. Figure 5 shows a comparison of predicted spectra from the various models to the experimental results of Bonness (2010), Martin and Leehey (1977) and Martini et al. (1984) and Smol'yakov and Tkachenko (1991). The figure shows that the widely used model, i.e. Corcos model, fails to predict the correct level of the spectra in the low wavenumber range. The Efimtsov model, which mimics the Corcos model to a large extent fails as well. Smol'yakov and Tkachenko's model under predicts the level, while the Witting model over predicts it. The Chase model predicts a rapid decrease in level at low wavenumbers. The level predicted by our model is in good agreement with all the data sets shown on the figure and hence outperforms all the models in the low wavenumber range.
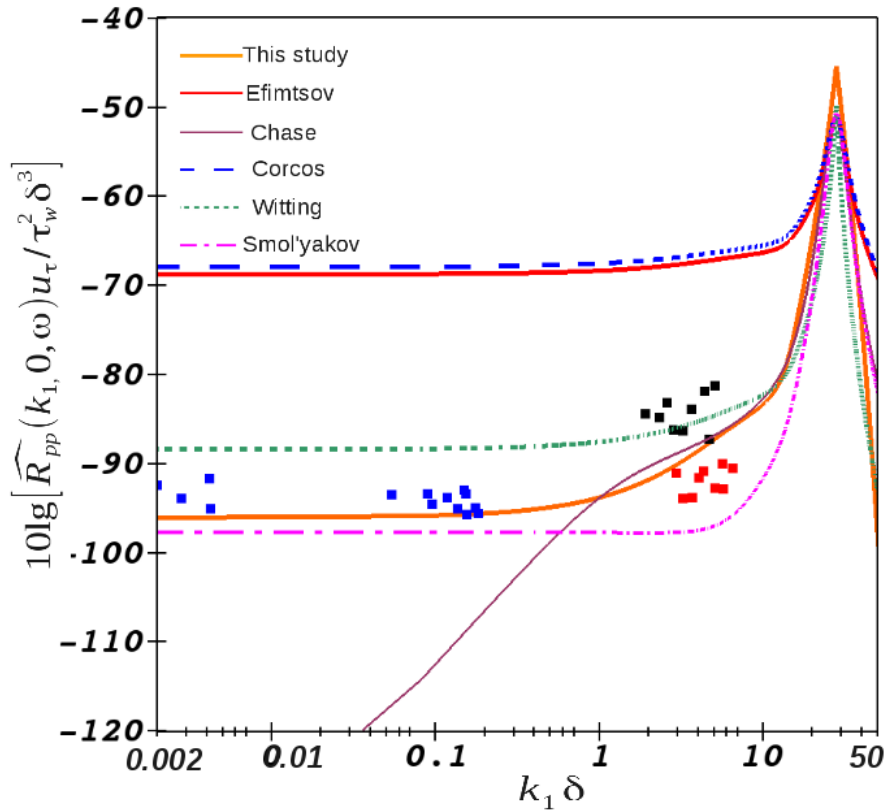

Figure 5: Comparison of predicted low wavenumber spectral level from various models. ■ Bonness (2010), ■ Martin and Leehey (1977) and Martini et al. (1984), ■ Smol'yakov (1991).

3.3 Two Dimensional Wavenumber-Frequency Spectra

A two dimensional spectrum, $\hat{R}_{pp}(k_1, \omega)$, is obtained by integration of a three dimensional spectrum

$$\hat{R}_{pp}(k_1, \omega) = \int \hat{R}_{pp}(k_1, k_2, \omega) \, dk_2 \tag{17}$$

which implies that the detailed contour shapes and convection bandwidth will affect the two dimensional spectra. Comparisons of two dimensional spectra obtained from our proposed model and from Corcos', Efimtsov, Smol'yakov and Tkachenko, Chase and Witting to the LES results of Viazzo et al. (2001) are shown on Figure 6(a)-(b) for dimensionless frequencies of $\frac{\omega \delta}{u_\tau} = 103$, Figure 6(a), and 203, Figure 6(b). The flow data used was that from Viazzo et al. (2001); $\frac{u_\tau}{U_\infty} = 0.048$ and $\frac{U_c}{U_\infty} = 0.65$. Given the results for the three dimensional spectra obtained from Corcos' and Efimtsov's models, section 3.1 above, it is no surprise that the level predicted for the two dimensional spectra at low wavenumbers by these two models is higher than that obtained from the LES results. For the two dimensionless frequencies of Figure 6, it can be concluded that the proposed model gives a better agreement with LES results for both frequencies. Given the steep decay of our three dimensional wavenumber-frequency spectrum for wavenumbers above the convective peak, the resulting two dimensional spectra have lower levels across the wavenumber range as shown of Figures. 6(a)-(b).
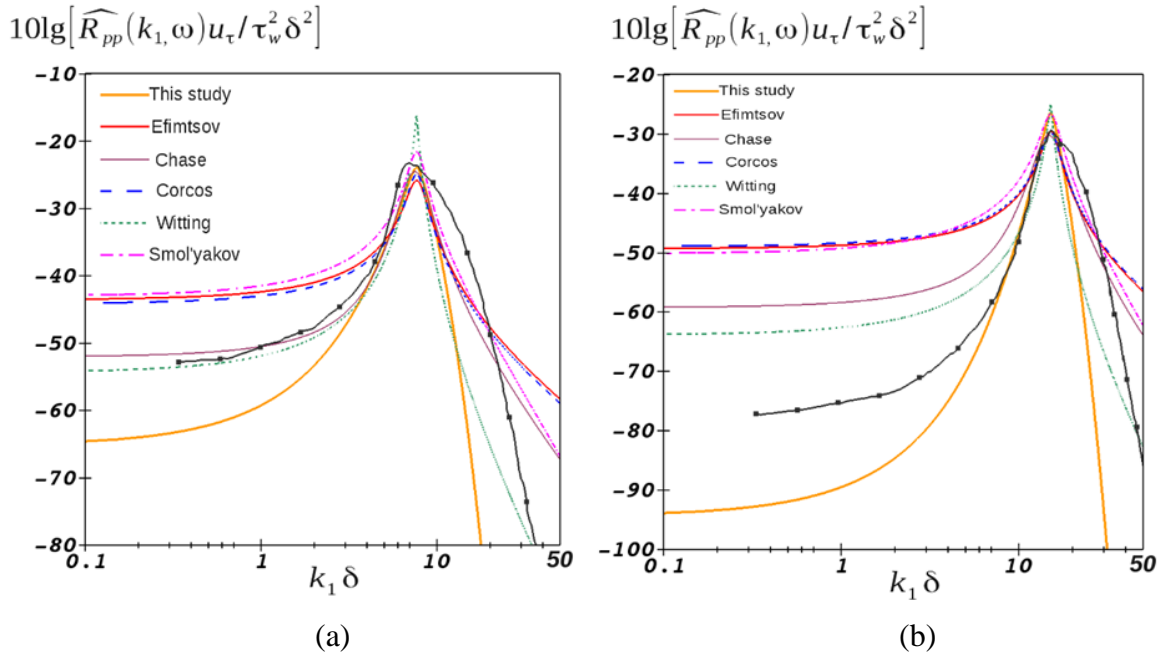

Figure 6: Two dimensional wavenumber-frequency spectra (a) $\frac{\omega \delta}{u_\tau} = 103$ and (b) $\frac{\omega \delta}{u_\tau} = 203$. The black line with symbols represents the LES results from Viazzo et al. (2001).

3.4 Contours of Wavenumber-Frequency Spectra Near the Convective Peak

The shape of the wavenumber-frequency spectra contours around the convective peak is of great importance to the problem of noise radiation especially at high speeds as pointed out by

Graham (1996). Hence it is critical to predict the shape of the contours correctly. Large Eddy Simulation results Gloerfelt and Berland (2013) showed that the contours are ellipses while Corcos' model predicts diamond shape contours with straight lines. Figure 7 shows the shape of the contours predicted by several models. Our proposed model shows elliptic shape contours, Figure 7(a), whereas Corcos', Figure 7(b), and Efimtsov, Figure 7(c), show diamond shape with straight line. The Chase model also shows elliptic shaped contours similar to our proposed model, Figure 7(d), however, Smol'yakov and Tkachenko model exhibits figure eight shaped contours, Figure 7(e), which are rather unusual. Witting's model predicts very narrow contours near the convective peak with sharp corners, Figure 7(f).
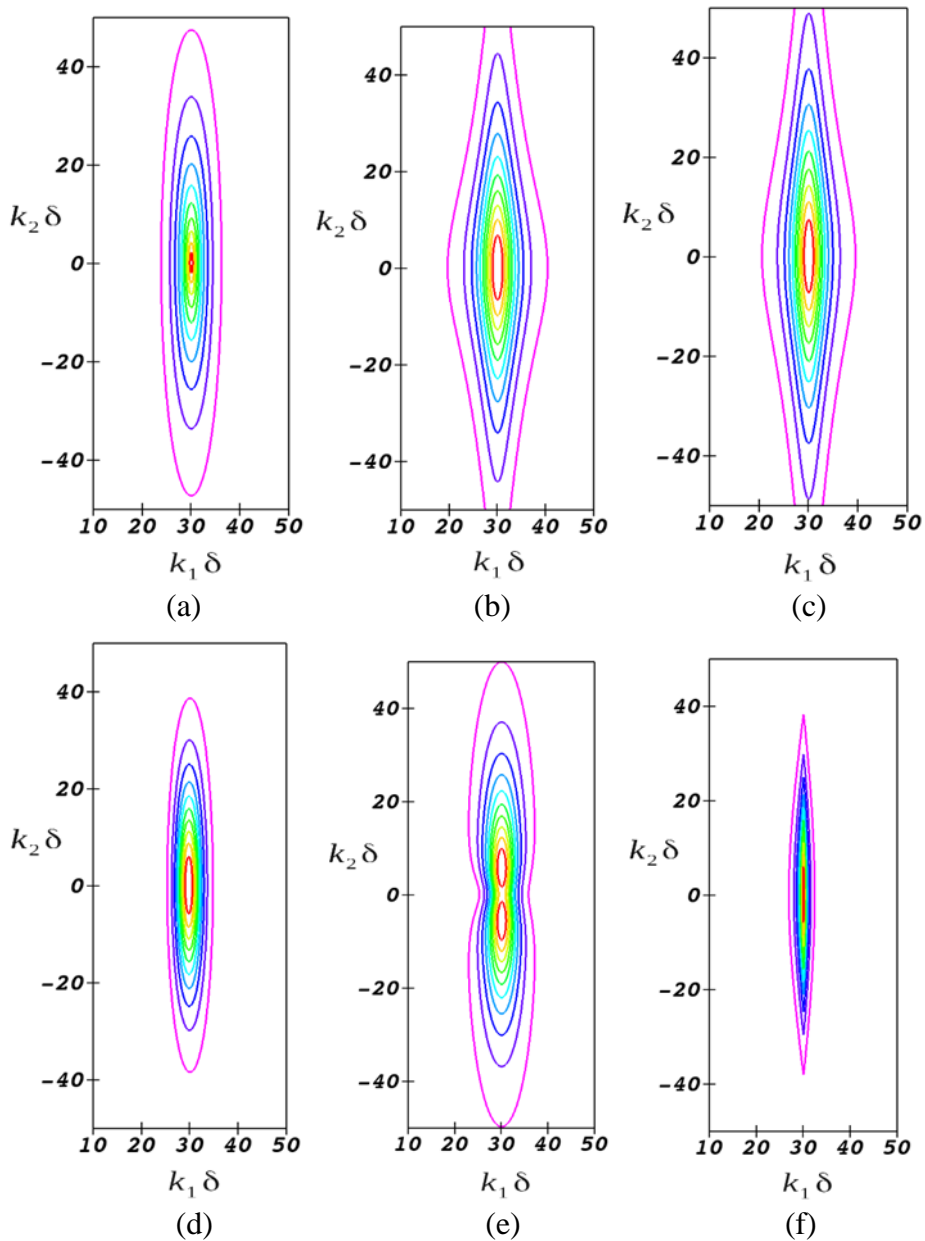

Figure 7: Comparison of the coherence contours in the wavenumber space for $\frac{\omega\delta}{u_\tau} = 727$.
(a) Our model, (b) Corcos, (c) Efimtsov, (d) Chase, (e) Smol'yakov and Tkachenko, (f) Witting.

3.5   Coherence Contours

Singer (1996b) carried out a large eddy simulation computation for $\frac{\omega\delta}{u_\tau} = 77.77(\frac{\omega\delta^*}{u_\tau} =$ 10.11) and flow quantities of $\frac{U_c}{u_\tau} = 16.5$ and $\frac{\delta^*}{\delta} = 0.13$. Figure 8(a) shows the coherence contours obtained from the Large Eddy Simulation in solid lines and the dashed lines obtained from the Corcos model represented by the product $A\left(\frac{\omega\zeta}{U_c}\right)B(\frac{\omega\eta}{U_c})$. It is clear from the figure that the solid lines are curved like ellipses and that the dashed lines are nearly straight lines. Figure 8(b) shows the coherence contours calculated using our model for the same parameters as those above. Our predicted contour shapes are in good agreement with those calculated using LES.

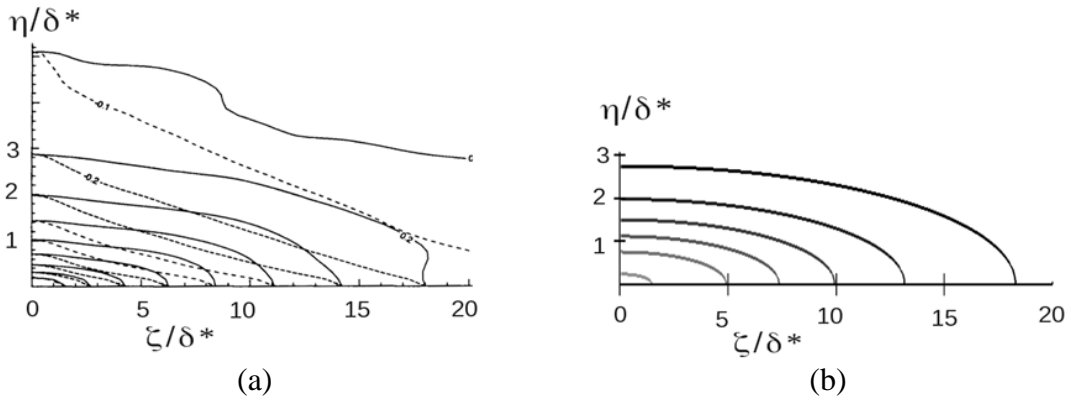(a)   (b)

Figure 8: Coherence contours with increments of 0.1 for $\frac{\omega\delta}{u_\tau} = 77.77$ ($\frac{\omega\delta^*}{u_\tau} = 10.11$). (a) solid line : LES results, dashed line: Corcos model. (b) Proposed model.

Figure 9 shows the coherence profile as a function of the dimensionless separation distance obtained using our model and that obtained from LES results of Singer (1996b). One should note that δ^* is small hence the difference between the model prediction and LES results is also small.
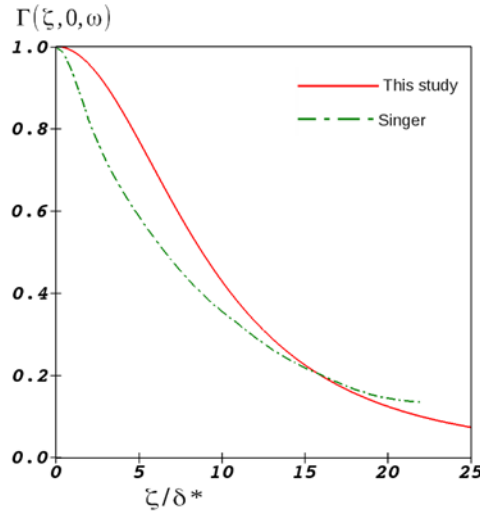

Figure 9: Comparison of coherence profiles, $\frac{\omega\delta}{u_\tau} = 77.77$ $\left(\frac{\omega\delta^*}{u_\tau} = 10.11\right)$.

4   Conclusions

In this paper, a new semi-empirical model of the wall pressure fluctuation has been presented. It is based on computational results, LES and DNS, and experimental measurements. The model improves on the Corcos (1963) and Efimtsov (1982) models that have been used extensively in various engineering applications. The improvements are in the correct shape of the coherence contours and the level of the spectra at low wavenumbers. The proposed spectrum maintains the simplicity of the Corcos (1963) model and has a mathematical formulation in both the wavenumber-frequency and space-frequency domains. All the testing performed on the model show better agreement with numerical and experimental results at various dimensionless frequencies.

Appendix A: Shape of Coherence Contours

The wall-pressure fluctuation is defined by the space-time covariance

$$R_{pp}(\zeta, \eta, \tau) = \langle p(x_1, x_2, t) p(x_1 + \zeta, x_2 + \eta, t + \tau) \rangle \tag{A.1}$$

and given the shape of $R_{pp}(\zeta, \eta, \tau)$, shown on Figure A-1, around the zero separation in ζ
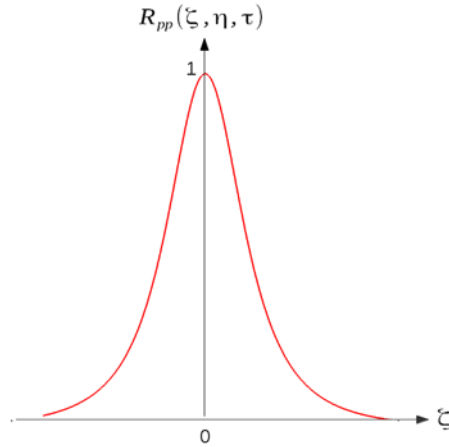

Figure A-1: Illustration of the WPF covariance as a function of the streamwise separation for a fixed spanwise and temporal separations.

then

$$R_{pp}(\zeta, \eta, \tau) = R_{pp}(-\zeta, \eta, \tau) \quad \text{and similarly} \quad R_{pp}(\zeta, \eta, \tau) = R_{pp}(\zeta, -\eta, \tau) \tag{A.2}$$

hence

$$\left. \frac{\partial R_{pp}(\zeta, \eta, \tau)}{\partial \zeta} \right)_{\zeta=0} = 0 \qquad \text{and} \qquad \left. \frac{\partial R_{pp}(\zeta, \eta, \tau)}{\partial \eta} \right)_{\eta=0} = 0. \tag{A.3}$$

The cross-spectrum can be written as

$$R_{pp}^*(\zeta, \eta, \omega) = \frac{1}{2\pi} \int R_{pp}(\zeta, \eta, \tau) e^{-i\omega\tau} d\tau \tag{A.4}$$

and the coherence is the defined as

$$\Gamma(\zeta, \eta, \omega) = \frac{R_{pp}^*(\zeta, \eta, \omega)}{R_{pp}^*(\omega)}. \tag{A.5}$$

Along the coherence contour lines $\Gamma(\zeta, \eta, \omega) = const.$, therefore using Equation (A.4) along with $\frac{\partial \Gamma}{\partial \zeta} = 0$ one arrives at

$$\int \left(\frac{\partial R_{pp}(\zeta, \eta, \tau)}{\partial \zeta} + \frac{\partial R_{pp}(\zeta, \eta, \tau)}{\partial \eta} \cdot \frac{d\eta}{d\zeta} \right) e^{-i\omega\tau} \, d\tau = 0 \tag{A.6}$$

and given that ω is arbitrary and for all separation times τ

$$\frac{\partial R_{pp}(\zeta, \eta, \tau)}{\partial \zeta} + \frac{\partial R_{pp}(\zeta, \eta, \tau)}{\partial \eta} \cdot \frac{d\eta}{d\zeta} = 0 \tag{A.7}$$

leading to

$$\frac{d\eta}{d\zeta} = - \frac{\partial R_{pp}(\zeta, \eta, \tau)/\partial \zeta}{\partial R_{pp}(\zeta, \eta, \tau)/\partial \eta}. \tag{A.8}$$

Using (A.3) into (A.8) leads to

$$\left. \frac{d\eta}{d\zeta} \right)_{\zeta=0} = 0 \qquad \text{and} \qquad \left. \frac{d\eta}{d\zeta} \right)_{\eta=0} = -\infty . \tag{A.9}$$

Equations (A.9) shows that the derivatives of the contour curve varies from 0, on the η axis, to $-\infty$, on the ζ axis, as shown on Figure A-2. If one assumes

$$\frac{d\eta}{d\zeta} = - \frac{1}{m^2} \frac{\zeta}{\eta} \tag{A.10}$$

then the coherence contour shapes are

$$\zeta^2 + (m\eta)^2 = r^2 \tag{A.11}$$

which represents a family of ellipses. For the Corcos (1963), the coherence is given by

$$\Gamma(\zeta, \eta, \omega) = A \left(\frac{\omega \zeta}{U_c} \right) B \left(\frac{\omega \eta}{U_c} \right) \tag{A.12}$$

with A and B given by Equation (3), then

$$\frac{d\Gamma}{d\zeta} = 0 = \frac{\partial A}{\partial \zeta} B + A \frac{\partial B}{\partial \eta} \frac{d\eta}{d\zeta} \tag{A.13}$$

which leads to

$$\frac{d\eta}{d\zeta} = - \frac{\alpha}{\beta}. \tag{A.14}$$

Indicating that the contour curves are parallel lines with a negative slope as shown on Figure A-2.
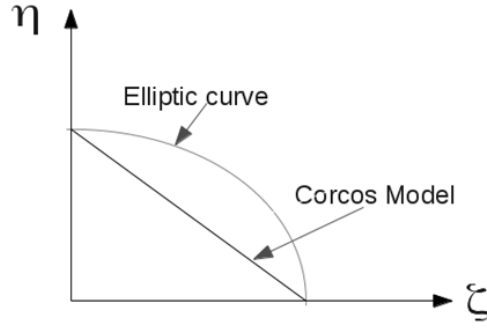
Figure A-2: Illustration of a coherence contour line

Appendix B: Derivation of the Cross-Spectrum

Starting from Equation (7)

$$\hat{R}_{pp}(k_1, k_2, \omega) = C_1 R_{pp}^*(\omega) e^{-\alpha r_k \delta} \quad \text{with} \quad C_1 = \alpha^2 m \delta^2 \frac{1}{2\pi} \tag{B.1}$$

The cross-spectrum is defined by

$$R_{pp}^*(\zeta, \eta, \omega) = \iint \hat{R}_{pp}(k_1, k_2, \omega) e^{i(k_1 \zeta + k_2 \eta)} dk_1 dk_2 \tag{B.2}$$

which after using Equation (B.1) becomes

$$R_{pp}^*(\zeta, \eta, \omega) = C_1 R_{pp}^*(\omega) \iint e^{-\tilde{\alpha} r_k} e^{i\left(k_1 - \frac{\omega}{U_c}\right)\zeta + i k_2 \eta} e^{i\frac{\omega}{U_c}\zeta} dk_1 dk_2$$
$$= C_1 R_{pp}^*(\omega) e^{i\frac{\omega}{U_c}\zeta} \iint e^{-\tilde{\alpha} r_k} e^{i\left(\tilde{k}_1 \zeta + \tilde{k}_2 \frac{\eta}{m}\right)} d\tilde{k}_1 d\tilde{k}_2. \tag{B.3}$$

In Equation (B.3), $\tilde{k}_1 = k_1 - \frac{\omega}{U_c}$ and $\tilde{k}_2 = m k_2$. Figure B-1 shows the polar coordinates used and defined by

$$|r_k|^2 = \left[k_1 - \frac{\omega}{U_c}\right]^2 + (m k_2)^2 \quad \text{and} \quad \theta = arctan\left(\frac{m k_2}{k_1 - \frac{\omega}{U_c}}\right). \tag{B.4}$$

Equation (B.3) becomes

$$R_{pp}^*(\zeta, \eta, \omega) = \frac{C_1}{m} R_{pp}^*(\omega) e^{i\frac{\omega}{U_c}\zeta} \int_0^{2\pi} \int_0^\infty e^{-\tilde{\alpha} r_k} e^{i r_k \left(\zeta cos\theta + \frac{\eta}{m} sin\theta\right)} r_k dr_k d\theta. \tag{B.5}$$

Let G represent the integral

$$G = \int_0^{2\pi} \int_0^\infty e^{-\tilde{\alpha} r_k} e^{i r_k \left(\zeta cos\theta + \frac{\eta}{m} sin\theta\right)} r_k dr_k d\theta = \int_0^{2\pi} \frac{d\theta}{\left[\tilde{\alpha} - i\left(\zeta cos\theta + \frac{\eta}{m} sin\theta\right)\right]^2}. \tag{B.6}$$
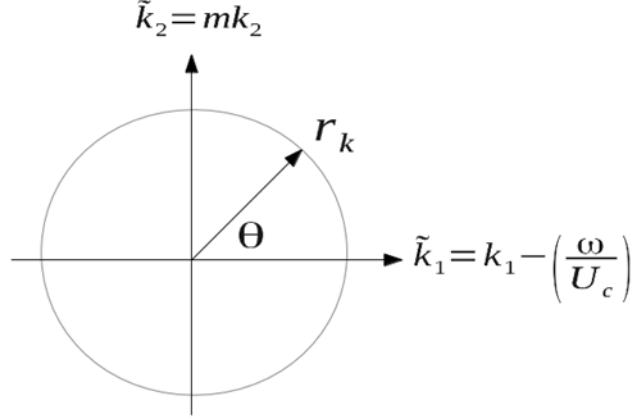
Figure B-1: The polar coordinate system.

The θ-integral will be carried-out in the complex plane using the method of residues. Let $z = e^{i\theta}$ then

$$d\theta = \frac{dz}{iz},$$
$$cos\theta = \frac{1}{2}\left(e^{i\theta} + e^{-i\theta}\right) = \frac{1}{2}\left(z + \frac{1}{z}\right) \text{ and } sin\theta = \frac{1}{2i}\left(e^{i\theta} - e^{-i\theta}\right) = \frac{1}{2j}\left(z + \frac{1}{z}\right). \quad (B.7)$$

As θ varies from 0 to 2π, the complex number z move in a counterclockwise direction on a unit circle, therefore G can be represented by

$$G = \int_0^{2\pi} \frac{d\theta}{\left[\tilde{\alpha} - i\left(\zeta cos\theta + \frac{\eta}{m}sin\theta\right)\right]^2} = \oint \frac{1}{\left[\tilde{\alpha} - i\frac{\zeta}{2}\left(z + \frac{1}{z}\right) - \frac{\eta}{2m}\left(z - \frac{1}{z}\right)\right]^2} \frac{dz}{iz} = \frac{4}{i}\oint \frac{zdz}{[(B+iA)z^2 - 2\tilde{\alpha}z - (B-iA)]^2}$$

$$= \frac{4}{i}\frac{1}{(B+iA)^2}\oint \frac{zdz}{\left[(z-z_0^+)(z-z_0^-)\right]^2} \quad (B.8)$$

with $A = \zeta$, $B = \frac{\eta}{m}$ and $z_0^{\pm} = \frac{\tilde{\alpha}}{B+iA} \pm \frac{\sqrt{\tilde{\alpha}^2 + B^2 + A^2}}{B+iA}$. Recognizing that z_0^- is a 2nd order pole

inside the unit circle and letting $f(z) = \frac{z}{\left(z-z_0^-\right)^2\left(z-z_0^+\right)^2}$, then using the residue theorem for $f(z)$ leads to

$$Res[f(z)] = \lim_{z \to z_0^-} \frac{d}{dz}\left[(z - z_0^-)^2 f(z)\right] = \lim_{z \to z_0^-} \frac{d}{dz}\left[\frac{z}{\left(z-z_0^+\right)^2}\right] = \frac{\tilde{\alpha}(B+iA)^2}{4(\tilde{\alpha}^2+B^2+A^2)^{\frac{3}{2}}} \quad (B.9)$$

and hence

$$G = \frac{4}{i}\frac{1}{(B+iA)^2} 2\pi i * Res[f(z)] = 2\pi \frac{\tilde{\alpha}}{(\tilde{\alpha}^2+B^2+A^2)^{\frac{3}{2}}}. \quad (B.10)$$

Substitution into Equation (B.5) with $\tilde{\alpha} = \alpha \cdot \delta$ leads to

$$R_{pp}^*(\zeta, \eta, \omega) = 2\pi \frac{C_1}{m\delta^2} R_{pp}^*(\omega) e^{i\frac{\omega}{U_c}\zeta} \frac{\alpha}{\left(\alpha^2 + \left(\frac{\eta}{m\delta}\right)^2 + \left(\frac{\zeta}{\delta}\right)^2\right)^{\frac{3}{2}}} \qquad (B.11)$$

For $\zeta = \eta = 0$ then

$$R_{pp}^*(0,0,\omega) = R_{pp}^*(\omega) = 2\pi \frac{C_1}{m\delta^2} R_{pp}^*(\omega) \frac{1}{\alpha^2} \quad \text{and} \quad C_1 = \alpha^2 m\delta^2 \frac{1}{2\pi} \qquad (B.12)$$

and hence

$$R_{pp}^*(\zeta, \eta, \omega) = \alpha^3 R_{pp}^*(\omega) e^{i\frac{\omega}{U_c}\zeta} \frac{1}{\left(\alpha^2 + \left(\frac{\eta}{m\delta}\right)^2 + \left(\frac{\zeta}{\delta}\right)^2\right)^{\frac{3}{2}}}. \qquad (B.13)$$

References

[1] B.M. Abraham, and W. L. Keith. "Direct Measurements of Turbulent Boundary Layer Wall Pressure Wavenumber-Frequency Spectra." Journal of Fluids Engineering 120 March (1998): 29–39.

[2] W.K. Bonness, D.E. Capone, S.A. Hambric, "Low-wavenumber turbulent boundary layer wall-pressure measurements from vibration data on a cylinder in pipe flow", Journal of Sound and Vibration 329 (2010) pp. 4166–4180.

[3] M.K. Bull, "Wall Pressure Fluctuations Beneath Turbulent Boundary Layers: Some Reflections on Forty Years of Research." Journal of Sound and Vibration 190.3 (1996): 299–315.

[4] A. Caiazzo, R. D'Amico, W. Desmet, "A Generalized Corcos model for modelling turbulent boundary layer wall pressure fluctuations" Journal of Sound and Vibration 372 (2016), 192-210.

[5] D.M. Chase, "Modeling the Wavevector-Frequency Spectrum of Turbulent Boundary Layer Wall Pressure." Journal of Sound and Vibration 70.1 (1980): 29–67.

[6] D.M. Chase, "The character of the turbulent wall pressure spectrum at subconvective wavenumbers and a suggested comprehensive model." Journal of Sound and Vibration 112 (1987): 125–147.

[7] H. Choi, and P. Moin. "On the Space–Time Characteristics of Wall- Pressure Fluctuations." Physics of Fluids A2 (1990): 1450– 1460.

[8] G.M. Corcos, "Resolution of Pressure in Turbulence." Journal of the Acoustical Society of America 35.2 (1963): 192–199.

[9] A.P. Dowling, "Flow noise on surfaces." Modern Methods in Analytical Acoustics. Great Britain: Springer-Verlag. (1992): 452.

[10] H. Eckelmann, "A review of knowledge on pressure fluctuatons." Proc. Zoran Zaric Memorial Intenanational Seminar on Near-Wall Turbulence, May 16-20 (1988) Dubrovnik, Yugoslavia.

[11] B.M. Efimtsov, "Characteristics of the Field of Turbulent Wall Pressure Fluctuations at Large Reynolds Numbers." Soviet Physics Acoustics 28.4 (1982): 289–292.

[12] T. Farabee, and M. J. Casarella. "Spectral Features of Wall Pressure Fluctuations beneath Turbulent Boundary Layers." Physics of Fluids 3.10 (1991): 2410–2420.

[13] J.E. Ffowcs Williams, "Boundary-layer pressures and the Corcos model: a development to incorporate low wavenumber constraints." Journal of Fluid Mechanics 125 (1982): 9–25.

[14] X. Gloerfelt, and J. Berland. "Turbulent boundary-layer noise: direct radiation at Mach number 0.5." Journal of Fluid Mechanics 723 (2013):318-351.

[15] M. Goody, "Empirical spectral model of surface pressure fluctuations." AIAA 42.9 (2004):1788-1794.

[16] W.R. Graham, "A comparison of models for the wavenumber-frequency spectra of turbulent boundary layer pressures." J. Sound and vibration 206.4 (1997): 541-565.

[17] Y.F. Hwang, and F. E. Geib. "Estimation of the wavevector-frequency spectrum of turbulent boundary layer wall pressure by multiple linear regression." Transactions of the American Society of Mechanical Engineers, Journal of Sound and Vibration, Acoustics, Stress and Reliability in Design 106 (1984): 334-342.

[18] D. Juve, M. Berton and E. Salze.."Spectral properties of wall-pressure fluctuations and their estimation from computational fluid dynamics." Flow induced Noise and Vibration Issues and aspects, Spring Intl publishing Switzerland 2015.

[19] D.J.J. Leclercq, and X. Bohineust. "Investigation and modeling of the wall pressure field beneath a turbulent boundary layer at low and medium frequencies." Journal of Sound and Vibration 257.3 (2002):477-501.

[20] N.C. Martin, and P. Leehey. J. Sound Vibration 52(1977):95.

[21] K.F. Martini, P. Leehey, and M. Moeller. "Comparison of techniques to measure the low wavenumber spectrum of a turbulent boundary layer." MIT Acoustics and Vibration Laboratory Rep. 92828-1: Cambridge, Mass. (1984).

[22] B.A. Singer, "Turbulent wall-pressure flucuations: new model for off-axis cross-spectral density", NASA Contractor Report 198297 (1996b).

[23] A.V. Smol'yakov, and V. M. Tkachenko. "Model of a field of pseudosonic turbulent wall pressures and experimental data." Soviet Physics Acoustics 37.6 (1991): 627–631.

[24] S. Viazzo, A. Dejoan , and R. Schiestel. "Spectral features of the wall-pressure fluctuations in turbulent wall flows with and without perturbations using LES." Int'l. J. of Heat and Fluid Flow 22 (2001):39-52.

[25] W.W Willmarth, "Pressure fluctuations beneath turbulent boundary layers." Annual Review of Fluid Mechanics 7 (1975): 13-38.

[26] W.W. Willmarth, and C.E. Wooldridge, "Measurements of the Fluctuating Pressure at the Wall Beneath a Thick Turbulent Boundary Layer." Journal of Fluid Mechanics 14 (1962): 187–210.

[27] J.M. Witting, "A spectral model of pressure fluctuations at a rigid wall bounding an incompressible fluid, based on turbulent structures in the boundary layer" Noise Control Eng. J. 26.1 (1986): 28-43.